

11. E. S. Boyden, F. Zhang, E. Bamberg, G. Nagel, K. Deisseroth, *Nat. Neurosci.* **8**, 1263–1268 (2005).
12. T. Ishizuka, M. Kakuda, R. Araki, H. Yawo, *Neurosci. Res.* **54**, 85–94 (2006).
13. X. Li *et al.*, *Proc. Natl. Acad. Sci. U.S.A.* **102**, 17816–17821 (2005).
14. A. R. Adamantidis, F. Zhang, A. M. Aravanis, K. Deisseroth, L. de Lecea, *Nature* **450**, 420–424 (2007).
15. A. M. Aravanis *et al.*, *J. Neural Eng.* **4**, S143–S156 (2007).
16. A. Berndt, M. Prigge, D. Gradmann, P. Hegemann, *Biophys. J.* **98**, 753–761 (2010).
17. G. Nagel *et al.*, *Proc. Natl. Acad. Sci. U.S.A.* **100**, 13940–13945 (2003).
18. J. Mattis *et al.*, *Nat. Methods* **9**, 159–172 (2012).
19. S. Geibel *et al.*, *Biophys. J.* **81**, 2059–2068 (2001).
20. A. Seki *et al.*, *Biophys. J.* **92**, 2559–2569 (2007).
21. A. Berndt, O. Yizhar, L. A. Gunaydin, P. Hegemann, K. Deisseroth, *Nat. Neurosci.* **12**, 229–234 (2009).
22. C. Bamann, R. Gueta, S. Kleinlogel, G. Nagel, E. Bamberg, *Biochemistry* **49**, 267–278 (2010).
23. O. Yizhar *et al.*, *Nature* **477**, 171–178 (2011).
24. H. E. Kato *et al.*, *Nature* **482**, 369–374 (2012).
25. S. Kleinlogel *et al.*, *Nat. Neurosci.* **14**, 513–518 (2011).
26. D. B. Sauer, W. Zeng, S. Raghunathan, Y. Jiang, *Proc. Natl. Acad. Sci. U.S.A.* **108**, 16634–16639 (2011).
27. B. Roux, R. MacKinnon, *Science* **285**, 100–102 (1999).
28. G. Yellen, *Nature* **419**, 35–42 (2002).
29. M. Köhler *et al.*, *Science* **273**, 1709–1714 (1996).
30. C. M. Nimigeon, J. S. Chappie, C. Miller, *Biochemistry* **42**, 9263–9268 (2003).
31. D. Bichet, M. Grabe, Y. N. Jan, L. Y. Jan, *Proc. Natl. Acad. Sci. U.S.A.* **103**, 14355–14360 (2006).
32. A. Berndt *et al.*, *Proc. Natl. Acad. Sci. U.S.A.* **108**, 7595–7600 (2011).
33. D. E. Clapham, C. Montell, G. Schultz, D. Julius; International Union of Pharmacology, *Pharmacol. Rev.* **55**, 591–596 (2003).
34. Single-letter abbreviations for the amino acid residues are as follows: A, Ala; C, Cys; D, Asp; E, Glu; F, Phe; G, Gly; H, His; I, Ile; K, Lys; L, Leu; M, Met; N, Asn; P, Pro; Q, Gln; R, Arg; S, Ser; T, Thr; V, Val; W, Trp; and Y, Tyr. In the mutants, other amino acids were substituted at certain locations; for example, E136R indicates that glutamic acid at position 136 was replaced by arginine.
35. Materials and methods are available as supplementary materials on Science Online.
36. H. Liske, X. Qian, P. Anikeeva, K. Deisseroth, S. Delp, *Sci. Rep.* **3**, 3110 (2013).
37. A. M. Herman, L. Huang, D. K. Murphey, I. Garcia, B. R. Arenkiel, *elife* **3**, e01481 (2014).
38. Y. Andrews-Zwilling *et al.*, *PLOS ONE* **7**, e40555 (2012).
39. J. Y. Lin, P. M. Knutsen, A. Muller, D. Kleinfeld, R. Y. Tsien, *Nat. Neurosci.* **16**, 1499–1508 (2013).
40. R. Prakash *et al.*, *Nat. Methods* **9**, 1171–1179 (2012).
41. J. L. Galzi *et al.*, *Nature* **359**, 500–505 (1992).
42. M. J. Gunthorpe, S. C. Lummis, *J. Biol. Chem.* **276**, 10977–10983 (2001).
43. H. Yang *et al.*, *Cell* **151**, 111–122 (2012).

**Acknowledgments:** We thank C. Perry and H. Swanson for technical assistance, the entire Deisseroth laboratory for helpful discussions, and T. Jardtzy for use of a Biotek Synergy4 plate reader. K.D. is supported by the National Institute of Mental Health, the Simons Foundation Autism Research Initiative, the National Institute on Drug Abuse, the Defense Advanced Research Projects Agency, the Gatsby Charitable Foundation, and the Wiegers Family Fund. A.B. received support from the German Academic Exchange Service (DAAD), and S.Y.L. received support from the Fidelity Foundation. Optogenetic tools and methods reported in this paper are distributed and supported freely ([www.optogenetics.org](http://www.optogenetics.org)).

#### Supplementary Materials

[www.sciencemag.org/content/344/6182/420/suppl/DC1](http://www.sciencemag.org/content/344/6182/420/suppl/DC1)  
Materials and Methods  
Figs. S1 to S3

18 February 2014; accepted 19 March 2014  
10.1126/science.1252367

# Neural Mechanisms of Object-Based Attention

Daniel Baldauf\* and Robert Desimone

How we attend to objects and their features that cannot be separated by location is not understood. We presented two temporally and spatially overlapping streams of objects, faces versus houses, and used magnetoencephalography and functional magnetic resonance imaging to separate neuronal responses to attended and unattended objects. Attention to faces versus houses enhanced the sensory responses in the fusiform face area (FFA) and parahippocampal place area (PPA), respectively. The increases in sensory responses were accompanied by induced gamma synchrony between the inferior frontal junction, IFJ, and either FFA or PPA, depending on which object was attended. The IFJ appeared to be the driver of the synchrony, as gamma phases were advanced by 20 ms in IFJ compared to FFA or PPA. Thus, the IFJ may direct the flow of visual processing during object-based attention, at least in part through coupled oscillations with specialized areas such as FFA and PPA.

When covertly attending to a location in the periphery, visual processing is biased toward the attended location, and the sources of top-down signals include the frontal eye fields (FEF) (1, 2) and parietal cortex (PC). FEF may modulate visual processing through a combination of firing rates and gamma frequency synchrony with visual cortex (2). For nonspatial attention, the mechanisms of top-down attention are much less clear. When people attend to a feature, such as a particular color (3–5), or to one of several objects at the same location (6–8), activity in the extrastriate areas representing properties of the attended object is enhanced. But where do the attentional biases (9) come from, and how do they enhance object processing when the distractors are not spatially separate?

We combined magnetoencephalography (MEG), supplemented by functional magnetic resonance imaging (fMRI) and diffusion tensor

imaging to optimize both spatial and temporal resolution. In the MEG experiment, two spatially overlapping streams of objects (faces and houses) were tagged at different presentation frequencies (1.5 and 2.0 Hz) (Fig. 1, A and B) (5, 10–12). The stimuli went in and out of “phase coherence,” so that they were modulated in visibility over time but did not change in luminance or flash on and off. When subjects were cued to attend to one of the streams and to detect occasional targets within the cued stream, frequency analyses allowed identifying brain regions that followed the stimulus oscillations.

Using MEG data only (13), the strongest activity evoked by the face tag was in the right fusiform gyrus, whereas the activity evoked by the house tag was more medially in the inferior-temporal cortex (IT) (Fig. 1C; figs. S1 and 2 for individual subjects and alternative source reconstruction approaches). These areas were roughly consistent with the locations of fusiform face area (FFA) and parahippocampal place area (PPA) determined previously in fMRI (14–16). To increase the accuracy of localization in each sub-

ject, we added high-resolution fMRI localizers for FFA and PPA (Fig. 2, B and D, and fig. S3A), which were focused at the expected spots (Fig. 2F).

To identify other areas important for nonspatial attention, we contrasted the brain state when attending to one of the two superimposed object classes with a similarly demanding state that did not require attending to either object class. The attention-related fMRI localizers revealed consistent activation in the inferior frontal junction (IFJ) at the intersection of the inferior-frontal and precentral sulcus (17–19) (Fig. 2, A, C, and E), with weaker and less-consistent signals in posterior-parietal and in inferior-temporal cortex (fig. S3C). A control experiment confirmed that IFJ’s activation was indeed related to nonspatial attention, rather than simply memory (fig. S4).

Each subject’s individual fMRI localizers were then used as regions of interest (ROIs) to guide the analysis of the MEG signals (see supplementary material for a description of the coregistration of fMRI and MEG). The modulation of sensory responses by attention in the tagging-frequency range is shown in Fig. 2G (fig. S5B for individual subjects). FFA and PPA had the strongest responses, with FFA more responsive to the attended face tag (*t* test,  $P < 0.001$ ) and PPA more responsive to the attended house tag (*t* test,  $P < 0.01$ ). Thus, object-specific attention modulates the sensory responses in FFA and PPA. Weaker sensory responses were found in region V1.

Although weaker in amplitude, sensory responses were also found in IFJ, and the attention effects were much stronger—there was a tagging frequency response only to the attended object (both *t* test,  $P < 0.001$ ). Control regions in the FEF (localized in separate fMRI runs, fig. S3D), PC (localized in the attention-related fMRI experiment in some participants) and the frontal pole (anatomically defined) showed only minor and less consistent responses. The general pattern of

McGovern Institute for Brain Research, Massachusetts Institute of Technology, Cambridge, 02139 MA, USA.

\*Corresponding author. E-mail: [baldauf@mit.edu](mailto:baldauf@mit.edu)

results did not depend on the specific tagging frequency assignment to faces or houses (fig. S5).

In temporal cortex, both MEG and fMRI results showed a moderate tendency of lateralization: FFA to the right and PPA to the left hemisphere (Fig. 2H).

The attentional effects in IFJ were slightly lateralized to the right.

We used Fourier transformations to extract the phase relation between the frequency-tag response and the stimulus on the screen, i.e., the latency of the

sensory responses (Fig. 2I). The phase lag of IFJ (corresponding to 208 ms) was shifted by about 25 ms in comparison to FFA and PPA (188 and 171 ms) (Fig. 2J and fig. S5) (20), which likely accounts for transmission time and synaptic delays between areas.

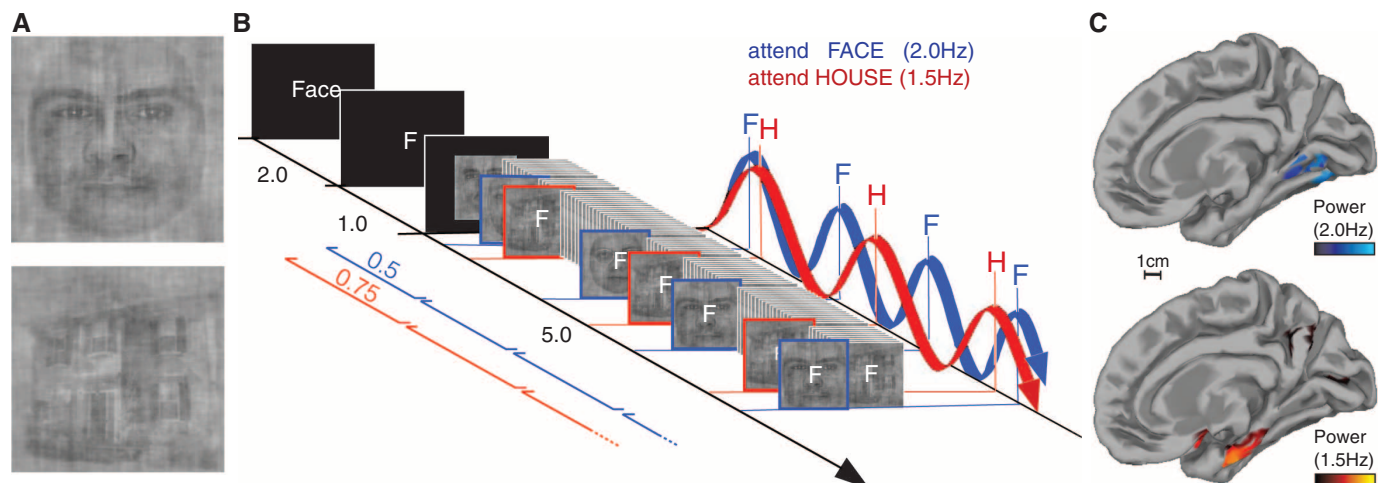


**Fig. 1. Stimuli and attention.** (A) Stimuli used in the MEG experiment (see online methods). (B) Sequence of stimuli consisting of an overlay of two streams of objects (faces and houses), fading in and out of a phase-scrambled noise mask at different

frequencies (1.5 and 2.0 Hz). Subjects had to attend the cued stream and report occasional 1-back repeats. (C) Fourier-transform of the minimum norm estimate when attending to faces (2.0 Hz) or houses (1.5 Hz,  $P < 0.05$ , FDR-corrected).

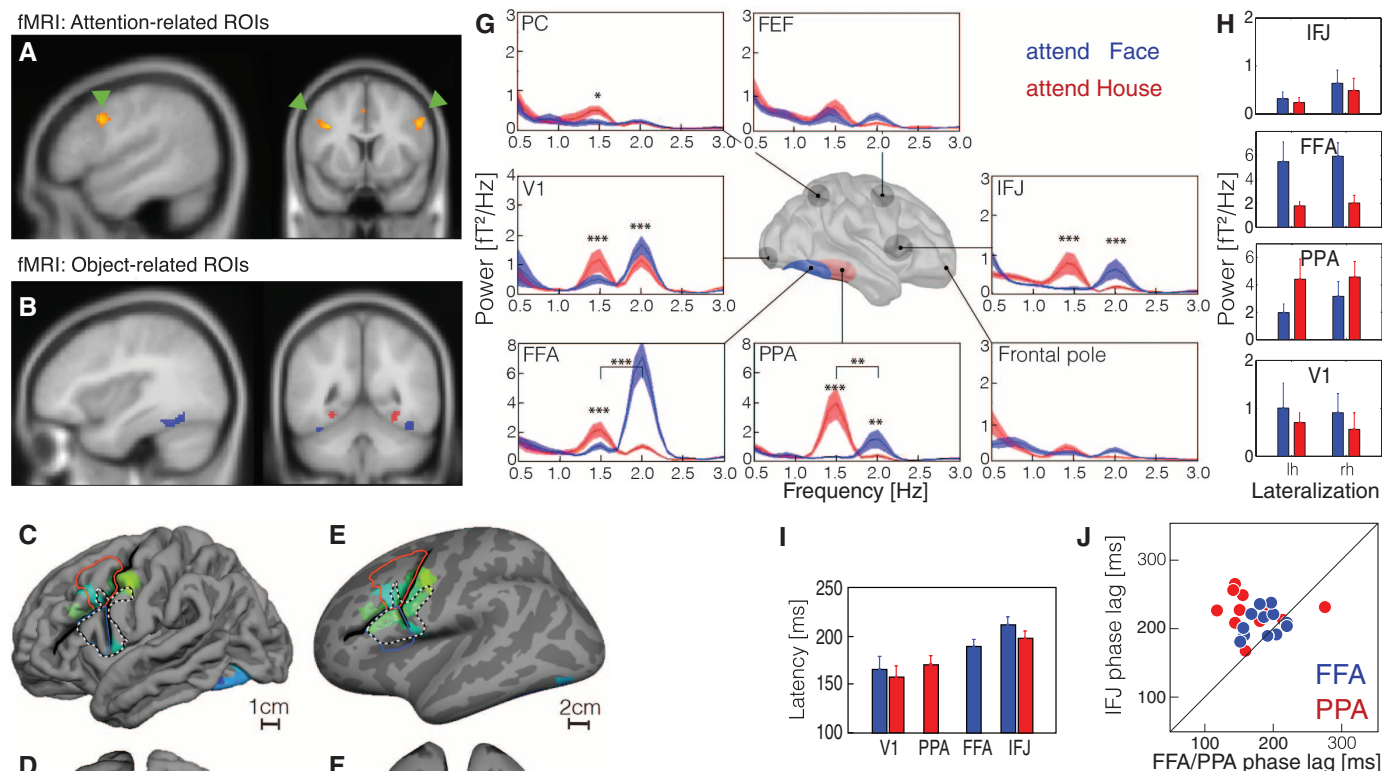


**Fig. 2. Measures of attention localization.** (A) Average of the fMRI localizers for attention-related and (B) object-related ROIs (blue: FFA, red: PPA,  $P < 0.001$ , FW error-corrected). (C and D) All subjects' individual ROIs superimposed on a standardized brain surface (red: middle frontal gyrus; blue: inferior frontal gyrus; dashed line: BA44) and (E) on an inflated brain. (F) Comparison of the average MEG-based (filled) and fMRI-based (outlines) localization of face- (blue) and house-related (red) activity. (G) Spectral power in the participants' individual ROIs when attending houses (1.5 Hz, red) or faces (2.0 Hz, blue). (H) Lateralization of the attentional effects. (I) Phase lags of the neural activity to the physical stimuli on screen. (J) Systematic phase advancement from FFA/PPA to IFJ.

To test for functional interactions among the areas, we analyzed coherence between the frontal and temporal ROIs (Fig. 3C) across a wide frequency spectrum, including frequency bands that were not time-locked to the stimuli (see time-frequency power spectra and an analysis of frequency nesting in fig. S6). The baseline-corrected coherence between IFJ-FFA (top) and IFJ-PPA (bottom) in the tagging-frequency range is shown in Fig. 3A. When attending into an area's preferred stimulus domain, that area became functionally connected with IFJ at the respective tagging frequency (both  $t$  test,  $P < 0.001$ ), as responses in both areas were phase-locked to the attended stimulus but with different phase lags.

Coherence at frequencies higher than the tagging frequency was dominated by shared background coherence, as typical in MEG. To reduce the influence of background coherence, we analyzed patterns of domain-specific coherence by computing an attention index, the

$$AIC = (\text{attend preferred} - \text{attend unpreferred}) / (\text{attend preferred} + \text{attend unpreferred})$$

which directly contrasts both attentional conditions and, therefore, is more sensitive to subtle attentional effects on coherence (Fig. 3B). When attending to faces (top, blue) coherence between IFJ and FFA increased not only at the tagging frequency (2.0 Hz) but also in a high-frequency band (70 to 100 Hz, both  $t$  test,  $P < 0.05$ ). Similarly, when attending to the house stimuli (red), IFJ and PPA exhibited increased coherence, both at the tagging frequency (1.5 Hz) and in a high-frequency band (60 to 90 Hz, both  $t$  test,

$P < 0.01$ ). In this high-frequency gamma range, the individual subjects varied considerably in their respective peak modulation frequency. As a check for whether the coherence in the gamma range resulted from common stimulus-locked onsets, we reran the analysis in a control data set, with shuffled trial order within each ROI (fig. S7C), which completely eliminated gamma coherence. Attentional modulations of coherence between IT and PC were weaker and nonsignificant (fig. S7D).

To test the directionality of the gamma-band coherence between IFJ and FFA/PPA, we analyzed the instantaneous phase lags between the two areas. Because portions of the signal in both sites are shared background coherence (due to electromagnetic field spread) or random noise, we first baseline-corrected the phase lag distributions to dissociate shared background coherence (which is simultaneous) and noise (which is uniformly distributed) from phase coherence that results from axonally transmitted synchronization (see supplementary methods and figs. S8 and S9). We then compared the residual phase lag distribution across a range of frequency bands around the subject's frequency of maximal coherence (peak  $\pm 10$  Hz). In most subjects (9 out of 12), the baseline-corrected phase lags systematically increased as a function of frequency, consistent with IFJ leading FFA/PPA with a constant time lag of about 20 ms (SE = 6 ms) (Fig. 3D and figs. S10 and S11). The three other subjects seemed to have stronger bottom-up or balanced coherence (see supplementary materials).

To determine whether IFJ is anatomically connected with FFA or PPA, we computed maps of probabilistic connectivities (21) to the seed regions

in FFA and PPA. When normalizing to the site of maximal activity within frontal cortex, both FFA- and PPA-connectomes revealed areas around IFJ to have the highest connection probabilities (see Fig. 3E and fig. S12).

The neural mechanism that enables attention to an object or feature seems intuitively more complex than spatial attention, which may only require a spatial-biasing signal that targets a relevant location. Yet the present study reveals some striking parallels in neural mechanisms: Prefrontal cortex seems to be a common source of top-down biasing signals, with FEF supplying signals for spatial attention and IFJ supplying signals for object or feature attention. With spatial attention, cells in FEF and visual cortex begin to oscillate together in the gamma frequency range, with FEF the “driver” in these oscillations (2). Here, we find that IFJ—although it has delayed sensory responses—is also the “driver” in coupled gamma oscillations with FFA/PPA. In primates, coherent gamma oscillations in FEF are phase-shifted by about 10 ms compared with oscillations in area V4, which has been argued to account for the axonal conduction time and synaptic delays between the two areas (2). With the phase shift, spikes of FEF cells presumably affect cells in V4 at a time of maximum depolarization, which increases their impact. Here, a phase shift of 25 ms may allow for longer transmission times from IFJ to FFA and PPA in humans. Thus, spikes originating from IFJ may arrive in FFA and PPA respectively, and vice versa, at a time of maximum depolarization in the receiving area, magnifying their impact. The directing of IFJ signals to the FFA versus PPA may not be inherently more

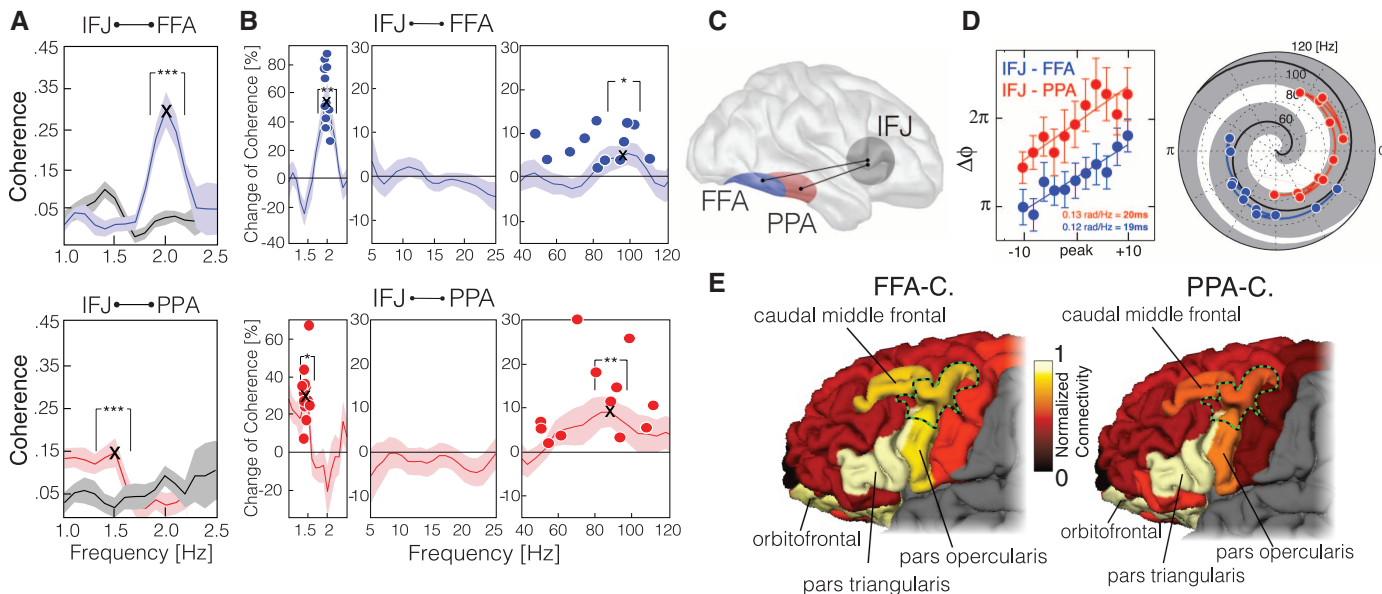


**Fig. 3. Coherence measures of attention.** (A) Cross-area coherence spectra. (B) Attention indices, converted into changes of coherence. When attending to the preferred stimulus (faces for FFA, houses for PPA), coherence between IFJ and the respective temporal area increased at the respective tagging frequency and in a high-frequency band (70 to 100 Hz). Dots represent subjects' peaks of attentional modulations. (C) Schematic of the fronto-temporal connectivity.

(D) Directionality measure of gamma phase-lags between IFJ and FFA/PPA in polar (right) and Cartesian (left) coordinates. In 9 of 12 subjects the phase-lag of FFA/PPA to IFJ increased linearly with increasing frequencies around the subject's peak of gamma coherence, consistent with IFJ cycles leading over FFA/PPA cycles. (E) Parcellation-based probability maps of frontal connectivity to FFA/PPA.



complex than shifting FEF signals between different locations in the visual field.

IFJ may include areas that function as general executive modules (22, 23). Also, IFJ is close to areas Ba45 and Ba46, homologs of which have been described in nonhuman primate recordings to encode information about object-categories in delayed match-to-sample tasks (23, 24). Indeed, the “attentional template” that specifies the relevant location or object in spatial or feature attention is hardly distinguishable from working memory for these qualities (9), which is known to involve prefrontal cortex (24). Coupled interactions between prefrontal areas and visual areas (25–31) could underlie many cognitive phenomena in vision, with shared neural mechanisms but variations in the site of origin and the site of termination.

### References and Notes

1. T. Moore, K. M. Armstrong, *Nature* **421**, 370–373 (2003).
2. G. G. Gregoriou, S. J. Gotts, H. Zhou, R. Desimone, *Science* **324**, 1207–1210 (2009).
3. S. Treue, J. C. Martínez Trujillo, *Nature* **399**, 575–579 (1999).
4. J. T. Serences, G. M. Boynton, *Neuron* **55**, 301–312 (2007).
5. M. A. Schoenfeld, J.-M. Hopf, C. Merkel, H.-J. Heinze, S. A. Hillyard, *Nat. Neurosci.* **17**, 619–624 (2014).
6. K. M. O’Craven, P. E. Downing, N. Kanwisher, *Nature* **401**, 584–587 (1999).
7. J. Duncan, *J. Exp. Psychol. Gen.* **113**, 501–517 (1984).
8. V. M. Ciaramitaro, J. F. Mitchell, G. R. Stoner, J. H. Reynolds, G. M. Boynton, *J. Neurophysiol.* **105**, 1258–1265 (2011).
9. R. Desimone, J. Duncan, *Annu. Rev. Neurosci.* **18**, 193–222 (1995).
10. R. Hari, M. Hämäläinen, S.-L. Joutsiniemi, *J. Acoust. Soc. Am.* **86**, 1033–1039 (1989).
11. P. Lakatos, G. Karmos, A. D. Mehta, I. Ulbert, C. E. Schroeder, *Science* **320**, 110–113 (2008).
12. L. Parkkonen, J. Andersson, M. Hämäläinen, R. Hari, *Proc. Natl. Acad. Sci. U.S.A.* **105**, 20500–20504 (2008).
13. M. S. Hämäläinen, R. J. Ilmoniemi, *Med. Biol. Eng. Comput.* **32**, 35–42 (1994).
14. N. Kanwisher, J. McDermott, M. M. Chun, *J. Neurosci.* **17**, 4302–4311 (1997).
15. D. Y. Tsao, S. Moeller, W. A. Freiwald, *Proc. Natl. Acad. Sci. U.S.A.* **105**, 19514–19519 (2008).
16. R. Epstein, N. Kanwisher, *Nature* **392**, 598–601 (1998).
17. M. Brass, J. Derrfuss, B. Forstmann, D. Y. von Cramon, *Trends Cogn. Sci.* **9**, 314–316 (2005).
18. T. P. Zanto, M. T. Rubens, A. Thangavel, A. Gazzaley, *Nat. Neurosci.* **14**, 656–661 (2011).
19. A. Gazzaley, A. C. Nobre, *Trends Cogn. Sci.* **16**, 129–135 (2012).
20. J. Liu, A. Harris, N. Kanwisher, *Nat. Neurosci.* **5**, 910–916 (2002).

21. Z. M. Saygin *et al.*, *Nat. Neurosci.* **15**, 321–327 (2011).
22. J. Duncan, *Trends Cogn. Sci.* **14**, 172–179 (2010).
23. E. Fedorenko, J. Duncan, N. Kanwisher, *Curr. Biol.* **22**, 2059–2062 (2012).
24. G. Rainer, W. F. Asaad, E. K. Miller, *Nature* **393**, 577–579 (1998).
25. F. Barceló, S. Suwazono, R. T. Knight, *Nat. Neurosci.* **3**, 399–403 (2000).
26. P. Fries, *Trends Cogn. Sci.* **9**, 474–480 (2005).
27. O. Jensen, J. Kaiser, J.-P. Lachaux, *Trends Neurosci.* **30**, 317–324 (2007).
28. A. K. Engel, P. Fries, W. Singer, *Nat. Rev. Neurosci.* **2**, 704–716 (2001).
29. T. Womelsdorf *et al.*, *Science* **316**, 1609–1612 (2007).
30. M. Siegel, T. H. Donner, R. Oostenveld, P. Fries, A. K. Engel, *Neuron* **60**, 709–719 (2008).
31. R. T. Canolty *et al.*, *Science* **313**, 1626–1628 (2006).

**Acknowledgments:** We thank J. Liang, D. Pantazis, M. Hämäläinen, D. Dilks, D. Osher, Y. Zhang, C. Triantafyllou, S. Shannan, S. Arnold, C. Jennings. Supported by NIH (P30EY2621) and NSF (CCF-1231216), both to R.D.

### Supplementary Materials

www.sciencemag.org/content/344/6182/424/suppl/DC1  
Materials and Methods  
Supplementary Text  
Figs. S1 to S13  
References (32–78)

8 October 2013; accepted 1 April 2014

Published online 10 April 2014;

10.1126/science.1247003

# A Chloroplast Retrograde Signal Regulates Nuclear Alternative Splicing

Ezequiel Petrillo,<sup>1\*</sup> Micaela A. Godoy Herz,<sup>1</sup> Armin Fuchs,<sup>2</sup> Dominik Reifer,<sup>2</sup> John Fuller,<sup>3</sup> Marcelo J. Yanovsky,<sup>4</sup> Craig Simpson,<sup>3</sup> John W. S. Brown,<sup>3,5</sup> Andrea Barta,<sup>2</sup> Maria Kalyna,<sup>2†</sup> Alberto R. Kornblihtt<sup>1‡</sup>

Light is a source of energy and also a regulator of plant physiological adaptations. We show here that light/dark conditions affect alternative splicing of a subset of *Arabidopsis* genes preferentially encoding proteins involved in RNA processing. The effect requires functional chloroplasts and is also observed in roots when the communication with the photosynthetic tissues is not interrupted, suggesting that a signaling molecule travels through the plant. Using photosynthetic electron transfer inhibitors with different mechanisms of action, we deduce that the reduced pool of plastoquinones initiates a chloroplast retrograde signaling that regulates nuclear alternative splicing and is necessary for proper plant responses to varying light conditions.

Light regulates about 20% of the transcriptome in *Arabidopsis thaliana* and rice (1, 2). Alternative splicing has been shown to modulate gene expression during plant devel-

opment and in response to environmental cues (3). We observed that the alternative splicing of *At-RS31* (Fig. 1A), encoding a Ser-Arg-rich splicing factor (4), changed in different light regimes, which led us to investigate how light regulates alternative splicing in plants.

Seedlings were grown for a week in constant white light to minimize interference from the circadian clock and then transferred to light or dark conditions for different times (see the supplementary materials). We observed a two- and four-fold increase in the splicing index (SI)—defined as the abundance of the longest splicing isoform relative to the levels of all possible isoforms—of *At-RS31* [mRNA3/(mRNA1 + mRNA2 + mRNA3)] after 24 and 48 hours in the dark, respectively (Fig. 1B). This effect was rapidly reversed when seedlings were placed back in light, with total recovery of the original SI in about 3 hours (Fig.

1C), indicating that the kinetics of the splicing response is slower from light to dark than from dark to light.

The light effect is gene specific (fig. S1) and is also observed in diurnal cycles under short-day conditions (Fig. 1D and fig. S2). Furthermore, three circadian clock mutants behaved like the wild type (WT) in the response of *At-RS31* alternative splicing to light/dark (fig. S3). Changes in *At-RS31* splicing are proportional to light intensity both under constant light and in short-day-grown seedlings (fig. S4).

Both red (660 nm) and blue (470 nm) lights produced similar results as white light (Fig. 1E). Moreover, *At-RS31* alternative splicing responses to light/dark are not affected in phytochrome and cryptochrome signaling mutants (5, 6), ruling out photosensory pathways in this light regulation (Fig. 1F and figs. S5 and S6).

Light-triggered changes in *At-RS31* mRNA patterns are not due to differential mRNA degradation. First, the light effect is not observed in the presence of the transcription inhibitor actinomycin D (Fig. 1G). Second, the effects are still observed in *upf* mutants, defective in the nonsense-mediated mRNA decay (NMD) pathway (7) (Fig. 1H and fig. S7). Third, overexpression of the constitutive splicing factor U2AF<sup>65</sup> (8) in *Arabidopsis* protoplasts mimics the effects of light on *At-RS31* alternative splicing (Fig. 1I).

*mRNA1* is the only isoform encoding a full-length *At-RS31* protein (9). *mRNA3* and *mRNA2* are almost fully retained in the nucleus (fig. S8). *mRNA1* levels decrease considerably in dark without significant changes in the total amount of *At-RS31* transcripts (Fig. 2A and fig. S9), which suggests that alternative splicing is instrumental

<sup>1</sup>Laboratorio de Fisiología y Biología Molecular, Departamento de Fisiología, Biología Molecular y Celular, IFIBYNE-CONICET, Facultad de Ciencias Exactas y Naturales, Universidad de Buenos Aires, Ciudad Universitaria, Pabellón 2, C1428EHA Buenos Aires, Argentina. <sup>2</sup>Max F. Perutz Laboratories, Medical University of Vienna, A-1030 Vienna, Austria. <sup>3</sup>Cell and Molecular Sciences, The James Hutton Institute, Invergowrie, Dundee, Scotland. <sup>4</sup>Fundación Instituto Leloir, IIBBA-CONICET, C1405BWE Buenos Aires, Argentina. <sup>5</sup>Division of Plant Sciences, University of Dundee at The James Hutton Institute, Invergowrie, Dundee, Scotland.

\*Present address: Max F. Perutz Laboratories, Medical University of Vienna, A-1030 Vienna, Austria.

†Present address: Department of Applied Genetics and Cell Biology, BOKU, University of Natural Resources and Life Sciences, Muthgasse 18, A-1190 Vienna, Austria.

‡Corresponding author. E-mail: ark@fbmc.fcen.uba.ar

## Neural Mechanisms of Object-Based Attention

Daniel Baldauf and Robert Desimone

*Science* **344** (6182), 424-427.

DOI: 10.1126/science.1247003 originally published online April 10, 2014

### House or Face?

The neural mechanisms of spatial attention are well known, unlike nonspatial attention. **Baldauf and Desimone** (p. 424, published online 10 April) combined several technologies to identify a fronto-temporal network in humans that mediates nonspatial object-based attention. There is a clear top-down directionality of these oscillatory interactions, establishing the inferior-frontal cortex as a key source of nonspatial attentional inputs to the inferior-temporal cortex. Surprisingly, the mechanisms for nonspatial attention are strikingly parallel to the mechanisms of spatial attention.

#### ARTICLE TOOLS

<http://science.sciencemag.org/content/344/6182/424>

#### SUPPLEMENTARY MATERIALS

<http://science.sciencemag.org/content/suppl/2014/04/09/science.1247003.DC1>

#### REFERENCES

This article cites 73 articles, 17 of which you can access for free  
<http://science.sciencemag.org/content/344/6182/424#BIBL>

#### PERMISSIONS

<http://www.sciencemag.org/help/reprints-and-permissions>

Use of this article is subject to the [Terms of Service](#)



Supplementary Material for

**Structure-Guided Transformation of Channelrhodopsin into a Light-Activated Chloride Channel**

Andre Berndt, Soo Yeun Lee, Charu Ramakrishnan, Karl Deisseroth\*

\*Corresponding author. E-mail: [deissero@stanford.edu](mailto:deissero@stanford.edu)

Published 25 April 2014, *Science* **344**, 420 (2014)  
DOI: 10.1126/science.1252367

**This PDF file includes:**

Materials and Methods

Figs. S1 to S3

## Materials and Methods

**Structural representations** Figures of the C1C2 (pdb: 3UG9 (24)) structure were generated using the PyMOL Molecular Graphics System, Version 1.7.0.1 (Schrödinger, LLC; *PNAS* **98**:10037-41, 2001).

**Point mutagenesis of C1C2** C1C2 mutations were introduced using the QuickChange<sup>TM</sup> Site-Directed mutagenesis kit (Agilent) and purified with QIAprep<sup>TM</sup> Spin Miniprep Kits (Qiagen) after transformation and amplification in *E. coli*. We used AAV vectors bearing the CaMKII $\alpha$  promoter for protein expression in neurons, and a pcDNA3.1 vector bearing the CMV promoter for expression in HEK cells. All clones were fused to the eYFP (enhanced yellow fluorescent protein) gene for fluorescence microscopy.

**Neuronal culture preparation and imaging** Primary hippocampal neurons were cultured from postnatal day 0 (P0) Spague-Dawley rat pups (Charles River). The CA1 and CA3 regions were isolated, digested with 0.4 mg/mL papain (Worthington), and plated onto 12 mm glass coverslips pre-coated with 1:30 Matrigel (Beckton Dickinson Labware), at a density of 65,000 cells per well in 24-well plates. The cultured cells were maintained in Neurobasal-A medium (Invitrogen) containing 1.25% FBS (HyClone), 4% B-27 supplement (Gibco), 2 mM Glutamax (Gibco) and 2 mg/ml fluorodeoxyuridine (FUDR, Sigma), and kept in a humid culture incubator with 5% CO<sub>2</sub> at 37°C.

Cells were transfected at 6-10 days *in vitro* (DIV). A DNA-CaCl<sub>2</sub> mix containing the following was prepared per each well to be transfected: 2  $\mu$ g of DNA (prepared using an endotoxin-free preparation kit (Qiagen)) 1.875  $\mu$ l 2M CaCl<sub>2</sub>, and sterile water to a total volume of 15  $\mu$ l. An additional 15  $\mu$ l of 2X filtered HEPES-buffered saline (HBS, in mM: 50 HEPES, 1.5 Na<sub>2</sub>HPO<sub>4</sub>, 280 NaCl, pH 7.05 with NaOH) was added per DNA-CaCl<sub>2</sub> mix, and the resulting DNA-CaCl<sub>2</sub>-HBS mix was incubated at room temperature for 20 minutes. During this time, the neuronal growth medium was removed from the wells and saved at 37°C, and replaced with 400  $\mu$ l pre-warmed minimal essential medium (MEM). Once the DNA-CaCl<sub>2</sub>-HBS mix incubation was complete, the mix was then added dropwise into each well, and the plates were kept in the culture incubator for 45-60 minutes. Afterwards, each well was washed three times with 1 ml of pre-warmed MEM, and then the MEM was replaced with the original neuronal growth medium. The transfected cells were then returned to the culture incubator until recordings.

For confocal images of opsin-eYFP-expressing neurons, coverslips of transfected cells expressing were fixed for 15 minutes in 4% paraformaldehyde and mounted with PVA-DABCO. Images were acquired with a Leica DM600B confocal microscope, and the same settings were used across images.

**Electrophysiological recordings in hippocampal neurons** The Spectra X Light engine (Lumencor) was coupled to the fluorescence port of an Olympus BX61WI microscope to detect eYFP expression and to deliver light for opsin activation. 475/15 and 632/22 filters

were used for blue light and red light respectively, and light power density through a 40X objective was measured with a power meter (ThorLabs).

Whole-cell recordings were obtained with patch pipettes (4-6 M $\Omega$ ) pulled from glass capillaries (Sutter Instruments) with a horizontal puller (P-2000, Sutter Instruments). The external recording solution contained (in mM): 135 NaCl, 4 KCl, 10 HEPES, 2 CaCl<sub>2</sub>, 2 MgCl<sub>2</sub>, 30 D-glucose, pH 7.3 with synaptic transmission blockers 25  $\mu$ M D-APV, 10  $\mu$ M NBQX. The internal solution recording solution contained (in mM): 140 K-gluconate, 10 HEPES, 10 EGTA, 2 MgCl<sub>2</sub>, pH 7.3. Measurements were corrected for the liquid junction potential of +16 mV. We used 3 M CsCl agar bridges for the reference electrode at all recordings. Series resistance was monitored throughout recordings for stability. Recordings were made using a MultiClamp700B amplifier (Molecular Devices), pClamp10.3 (Molecular Devices), OriginLab8 (OriginLab), and Sigmaplot (SPSS) software was used to record and analyze data.

The stationary photocurrent upon light activation was used as the measure of photocurrent amplitude at different membrane potentials. The reversal potential ( $V_{rev}$ ) was defined as the point where the stationary photocurrent amplitude was 0 pA. Action potential threshold was measured at the voltage deflection point at which the first-order derivative of the membrane potential (dV/dt) exhibited a sharp transition, typically > 10 mV/ms. The resting membrane potential of the cell was measured in current-clamp after attaining whole-cell configuration. Input resistance was calculated from the steady-state current responses evoked by 20 mV hyperpolarizing steps in voltage-clamp. To investigate action potential inhibition, we tested opsin-expressing cells under two different spike induction protocols. Spikes were electrically evoked with intracellular current injections, either with short electrical pulses (30 ms pulse width, 50-280 pA) 10 Hz, or with a continuous 3 s electrical pulse. Light was applied for 1 s (during the 10 Hz train) or 0.5 s (during the continuous pulse) during the middle of the electrical current injection. Spike inhibition probability was calculated as the fraction of electrically-evoked spikes that were blocked during the light pulse epoch of the electrical stimulation.

**HEK cell culture preparation** Human embryonic kidney cell cultures (HEK-293: ATCC<sup>®</sup> CRL-1573<sup>™</sup>) were maintained in 50 ml Dulbecco's Modified Eagle Medium (Life Technologies) containing 100 units/mL of penicillin and 100  $\mu$ g/mL of streptomycin as well as fetal bovine serum at a dilution of 1:10. HEK cells were grown in incubators at 37 °C / 5% CO<sub>2</sub> and were transferred to a new 225 cm<sup>2</sup> culture flask (Thermo) every 3 to 4 days at passaging dilutions ranging from 1:5 to 1:8. 24h prior to DNA transfections cells were plated on 2 cm poly-D-lysine coated glass cover slips and maintained in 24 well culture plates (Thermo) with 500  $\mu$ l growth medium. 24h prior to recordings, HEK cells were transfected with 1.6  $\mu$ l plasmid DNA per well using 2  $\mu$ l Lipofectamine 2000 (Life Technologies).

**HEK cell electrophysiology** ChR-expressing cells were identified by eYFP fluorescence and recorded ~18 to 30 hours after transfection. We used the same equipment and methods as for neurons. Measurements were conducted in voltage clamp at membrane potentials between -75 and +55 mV. An external 3M CsCl agar bridge was used in all



recordings. We first characterized all constructs using the same internal and external solution as in neurons and corrected for the corresponding junction potential, and used stationary photocurrents for data analysis. The activation spectra for C1C2, iC1C2 and NpHR was determined by measuring stationary photocurrents at -75 mV in response to low light intensities at 0.65 mW/mm<sup>2</sup> in order to prevent saturation. We used 20 nm bandpass filters (Thorlabs) to apply light at different wavelengths (in nm): 400, 420, 440, 460, 470, 480, 490, 500, 520, 540, 560, 570, 580, 590, 600, 620, 630, 650. All photocurrent were normalized to reference values at 470 nm (C1C2 and iC1C2) or 570 nm (NpHR). Kinetics of channel closure were quantified by fitting photocurrents after light-off with mono-exponential functions in order to obtain corresponding tau<sub>off</sub> values. Light sensitivity measurements were carried out at 470 nm (C1C2, iC1C2) or 560 nm (NpHR). We applied light at intensities from 0.0021 to 5 mW/mm<sup>2</sup> and normalized corresponding photocurrents to the value at maximum light intensity.

We determined ion selectivities by varying ion composition and pH of the internal and external solutions. External solutions contained (in mM) 2 CaCl<sub>2</sub>, 2 MgCl<sub>2</sub>, 120 NaCl, 120 CsCl or 120 Na-gluconate, 10 Citric acid/Na-citrate (pH 6) or 10 HEPES (pH 7.3) or 10 Tris (pH 9). Internal solutions contained (in mM) 2 CaCl<sub>2</sub>, 2 MgCl<sub>2</sub>, 120 KCl, 120 CsCl or 120 K-gluconate, 10 Citric acid/Na-citrate (pH 6) or 10 HEPES (pH 7.3) or 10 Tris (pH 9). We corrected for junction potential under each condition (in mV): KCl<sub>int</sub>/NaCl<sub>ext</sub> = 4, KCl<sub>int</sub>/CsCl<sub>ext</sub> = -0.6, KCl<sub>int</sub>/NaGluc<sub>ext</sub> = -6.2, KGluc<sub>int</sub>/NaCl<sub>ext</sub> = 15.8, CsCl<sub>int</sub>/NaCl<sub>ext</sub> = 4.6. We used the Nernst equation to determine the Nernst potential for cations, Cl<sup>-</sup> and protons under each external and internal ion composition and pH. We used an adapted Goldman-Hodgkin-Katz equation to calculate the ratio of proton to Cl<sup>-</sup> permeability in iC1C2. We assumed that permeability for Na<sup>+</sup> and K<sup>+</sup> is zero, which resulted in:

$$V_{rev} = \frac{RT}{F} \ln \frac{P_H[H^+]_{ext} + P_{Na}[Na^+]_{ext} + P_K[K^+]_{ext} + P_{Cl}[Cl^-]_{int}}{P_H[H^+]_{int} + P_{Na}[Na^+]_{int} + P_K[K^+]_{int} + P_{Cl}[Cl^-]_{ext}}$$

$$V_{rev} = \frac{RT}{F} \ln \frac{P_H[H^+]_{ext} + P_{Cl}[Cl^-]_{int}}{P_H[H^+]_{int} + P_{Cl}[Cl^-]_{ext}}$$

$$\alpha = \frac{P_{Cl}}{P_H}$$

$$V_{rev} = \frac{RT}{F} \ln \frac{[H^+]_{ext} + \alpha[Cl^-]_{int}}{[H^+]_{int} + \alpha[Cl^-]_{ext}}$$

R = Gas constant, F = Faraday constant, T = absolute temperature

Statistical analysis was performed with a t-test or a two-way ANOVA, and a Mann-Whitney test for non-parametric data, using Origin8 (OriginLab) and Sigmaplot (SPSS) software. Data is presented as mean ± s.e.m., and error bars indicate s.e.m. p<0.05 is defined to be statistically significant.

[illegible]

### Figure S1

Protein alignment of C1C2 and iC1C2 in comparison to channelrhodopsin-2 (ChR2). The mutated residues of iC1C2 are highlighted in red and shown in relation to the transmembrane helices (TM 1-7) of C1C2 (gray bars) (24). Positioning of SwiChR mutations is shown in blue.

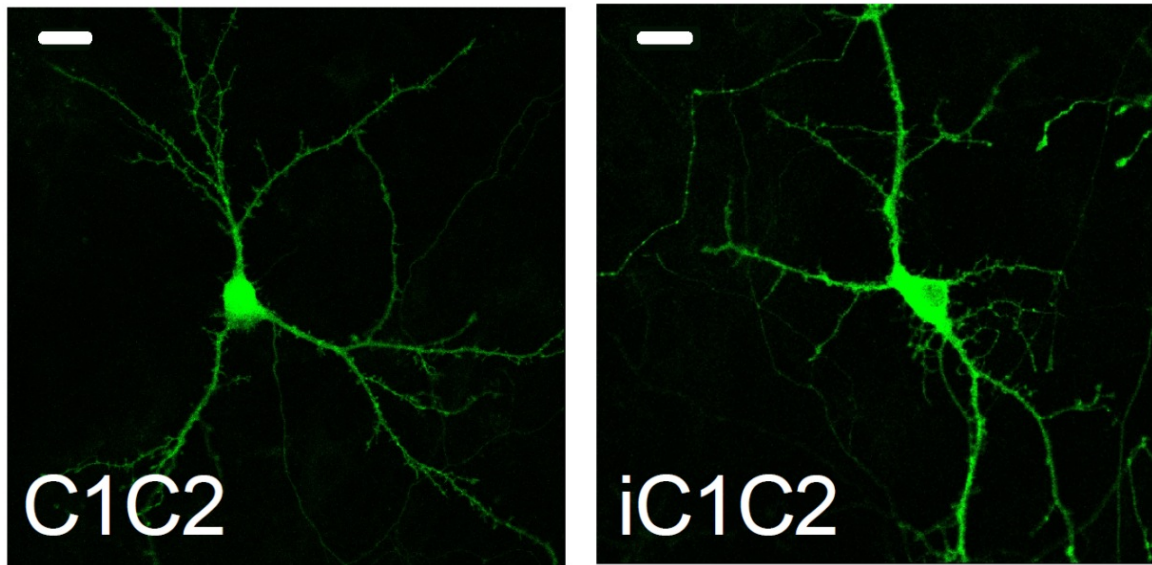


**Figure S2**

Confocal images of cultured neurons expressing C1C2-eYFP (left) and iC1C2-eYFP (right). Scale bar: 20  $\mu$ m.

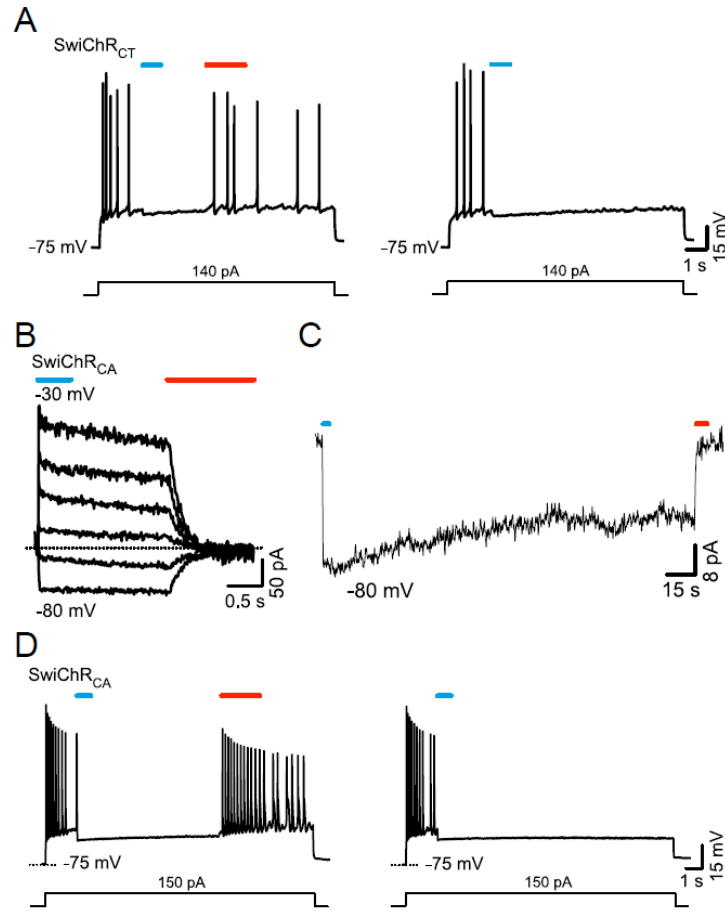


**Figure S3**

Bistable inhibition with SwiChRs. **(A)** Bistable spiking modulation with SwiChR<sub>CT</sub>. Spiking was induced by a continuous electrical pulse (3 s), stably inhibited by 475 nm light (blue bar) delivered at 5 mW/mm<sup>2</sup>, and resumed after 632 nm light application (red bar) (left). Prolonged spiking modulation in the same cell after only 475 nm light delivery (blue bar) at 5 mW/mm<sup>2</sup> (right) with the same current injection as in left panel. **(B)** Current-voltage relationship of SwiChR<sub>CA</sub> recorded at membrane potentials from -80 mV to -30 mV upon 470 nm activation pulses (blue bar) followed by 632 nm (red bar) light pulses. **(C)** Representative photocurrent of SwiChR<sub>CA</sub> upon 470 nm activation (blue bar) followed by a second light pulse at 632 nm (red bar). Light power density was 5 mW/mm<sup>2</sup>. **(D)** (left) Bistable spiking modulation by SwiChR<sub>CA</sub>. Spiking was induced by a continuous electrical pulse (3 s) and stably inhibited by 475 nm light (blue bar) delivered at 5 mW/mm<sup>2</sup>. Spiking resumed after 632 nm light application (red bar). **(E)** Prolonged spiking modulation of SwiChR<sub>CA</sub> of the same cell as in (D) with 475 nm light (blue bar) only, delivered at 5 mW/mm<sup>2</sup>; the same current injection was used to induce spiking as in (D).